ENG. Struct. Civ. Eng. 2026, 20(4): 674–689
https://doi.org/10.1007/s11709-026-1293-9

RESEARCH ARTICLE

Mechanistic insights into the strength and slaking resistance enhancement of biocemented sand through xanthan gum-assisted $CaCO_3$ nucleation

Sai ZHANG, Jianwen DING*, Shoujie WANG, Kexiang ZHANG, Xinrui ZHANG

Institute of Geotechnical Engineering, School of Transportation, Southeast University, Nanjing 211189, China
**Corresponding author. E-mail: jwding@seu.edu.cn*

ABSTRACT To address the limited reinforcement efficiency of enzyme-induced calcium carbonate precipitation (EICP) caused by insufficient nucleation sites, this study introduces xanthan gum (XG) to immobilize the enzyme and promote the $CaCO_3$ nucleation. A series of unconfined compressive strength (UCS) tests and ultrasonic oscillation tests were conducted to evaluate the effects of XG on the mechanical behavior and slaking resistance of biocemented sand. The nucleation and cementation mechanisms of XG addition were clarified through scanning electron microscopy with energy-dispersive spectroscopy and X-ray diffraction. The results demonstrate that as the XG concentration increased from 0 to 2 g/L, the UCS increases from 121.10 to 231.05 kPa, showing an increase of 90.8%. At the same time, the average slaking index decreases from 2.588 to 1.323. The enhancement is attributed to the increased viscosity of the enzyme solution with XG addition, which improves solution retention in low-energy sites. In addition, the negatively charged carboxylate groups on XG enhance Ca^{2+} adsorption, creating more nucleation sites and promoting targeted precipitation of $CaCO_3$ at particle contact points and interfaces. This study confirms that biopolymer-assisted nucleation can improve both the strength and slaking resistance of biocemented sand, providing a basis for promoting biocementation technologies in applications such as erosion control and hydrological engineering.

KEYWORDS EICP, XG, strength, slaking resistance, microscopic mechanism

1 Introduction

During the long-term service of soil structures, water-induced erosion frequently poses a significant challenge [1]. However, conventional soil stabilization techniques often struggle to achieve a balance between reinforcement effectiveness, ecological sustainability, and minimal environmental disturbance [2]. Therefore, it is imperative to adopt new efficient measures to enhance the workability of soils, especially their strength and slaking resistance [3–5]. To address this technical challenge, microbial mineralization was proposed and has emerged as a promising biogeotechnical solution [6,7]. This technique catalyzes the hydrolysis of urea through enzyme or enzyme-producing bacteria, producing CO_3^{2-} that react with Ca^{2+} to precipitate $CaCO_3$, which acts as a bonding agent between soil particles [8,9]. Actually, the precipitated $CaCO_3$ exists in soils in three modes: cementation mode, coating mode, and pore-filling mode [10]. The cementation mode refers to $CaCO_3$ preferentially forming at particle contact points to enhance structural integrity, as well as the coating mode involves gradual accumulation of $CaCO_3$ on particle surfaces, which may further evolve into the cementation mode. Therefore, promoting the preferential deposition of $CaCO_3$ at particle contacts and on particle surfaces is crucial for improving the mechanical performance and slaking resistance of biocemented soils.

Locations where a liquid can remain more stably due to the combined effects of surface forces, electrostatic forces, van der Waals forces, and capillary forces are referred to as low-energy sites, such as particle contact points and surface depressions [11]. According to colloid filtration theory, when polymer-based colloidal solutions

Article history: Received May 29, 2025; Accepted Dec 3, 2025

migrate through porous media, part of the colloids tends to accumulate at low-energy sites due to filtration effects and adsorption interactions [12]. Based on this principle, using colloids as carriers to immobilize bacteria or enzyme cannot only enhance their retention on the soil, but also effectively promote the deposition of $CaCO_3$ at particle contacts and interfaces [13]. Ma et al. [14] introduced kaolinite into bacterial solution to construct a microbially immobilized colloid system, which improved bacterial adsorption and retention in coarse sand, leading to a more uniform distribution of $CaCO_3$ precipitates. As a result, the unconfined compressive strength (UCS) and the impermeability of the biocemented coarse sand were improved. Similarly, other researchers have proposed the addition of polymer such as chitosan, polyvinyl alcohol and milk powder to further strengthen the immobilization of bacteria or enzyme within porous media [15–17]. These additives assist in the nucleation and precipitation of $CaCO_3$, demonstrating considerable potential for practical geotechnical engineering applications.

Moreover, in terms of enzyme-induced calcium carbonate precipitation (EICP), the enzyme exists in a free state and lacks the complex biotic interfacial regulation, which often results in disordered precipitation of $CaCO_3$, thereby leading to insufficient densification of the cementation and limited mechanical performance [18,19]. In contrast, during microbially induced calcium carbonate precipitation, microbial cell walls and their secreted extracellular polymeric substances (EPS) not only provide abundant nucleation sites but also regulate crystal growth, promoting the formation of densely structured, morphologically uniform, and strongly adherent $CaCO_3$ crystals [20,21]. Based on these differences, the introduction of EPS into the EICP system can create a stable immobilized colloidal matrix, which not only enhances the retention of enzyme, but also provides additional nucleation sites for $CaCO_3$ precipitation, thereby improving the solidification efficiency and mechanical enhancement of EICP-treated soils.

The commonly used EPS in microbial mineralization include chitosan, xanthan gum (XG), and guar gum [15,22–24]. The chains of these polymers interact with soil particles through electrostatic adsorption, hydrogen bonding, or physical filling, thereby enhancing soil strength, increasing particle cohesion, reducing permeability, improving durability, and altering compaction characteristics [25,26]. Among them, XG is a natural anionic polysaccharide secreted by Xanthomonas campestris, which exhibits high viscosity, excellent rheological properties, and outstanding freeze–thaw stability [27]. Meanwhile, XG can fill pores with colloidal phase under saturated conditions, as well as bond soil particle by forming fibrous or network-like structures under dry conditions, thereby substantially enhancing the workability of the soil [28,29]. Theoretically, XG can strengthen bonding in soils through a triple mechanism: 1) direct physical adhesion to soil particles; 2) promoting the enrichment and retention of the enzyme at low-energy sites within the soil; 3) providing nucleation sites for $CaCO_3$ precipitation. These synergistic effects collectively improve the strength and slaking resistance of EICP-treated soils.

Previous studies have indicated that the addition of XG can enhance the workability of soils such as soil mechanical properties and wind erosion resistance due to its intrinsic viscosity [24,30,31]. However, the potential of XG in assisting $CaCO_3$ nucleation has not been thoroughly investigated, and the influence of XG on the slaking resistance of biocemented soils under water-induced conditions remains insufficiently understood. Therefore, this study employs XG as a carrier to construct an immobilized enzyme colloidal system in sand grouting reinforcement, the reinforcement effectiveness and mechanisms of XG are investigated through a series of laboratory tests. First, the UCS tests were performed to investigate the strength evolution of biocemented sand under various XG concentrations. Subsequently, ultrasonic oscillation (UO) tests were utilized to assess the slaking behavior of particles from different sections of the biocemented specimen in water environments. In addition, calcium carbonate content (*CCC*) was measured and the relationships between *CCC*, UCS and slaking index (*SI*) were established. Finally, scanning electron microscopy (SEM) with energy-dispersive spectroscopy (EDS) and X-ray diffraction (XRD) analyses were conducted to reveal the microstructural distribution and mineralogical composition of $CaCO_3$. The investigation systematically clarifies the synergistic enhancement effects of biopolymer-based immobilization on $CaCO_3$ precipitation, UCS and slaking resistance, providing a basis for promoting bio-cementation technologies in applications such as erosion control and hydrological engineering.

2 Experimental details and testing procedure

2.1 Materials

The sand used in this study was sourced from Pingtan, Fujian Province, China, with a specific gravity of 2.65. The particle size distribution of the sand was measured through sieving method according to ASTM D422-63 [32], as shown in Fig. 1. The SEM observation reveals that the sand particles were relatively uniform in size, with surface depressions and irregular microstructures, which may provide additional attachment sites for EICP. The sand was rinsed with water to remove surface impurities, then oven-dried at 105 °C for 24 h. After cooling, it was stored in sealed containers for later use.

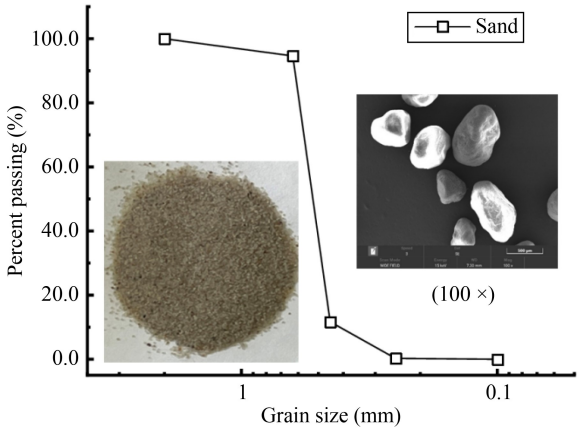

Fig. 1 Basic physical properties of sand.

The XG used in this study is a white, powdery biopolymer produced by the fermentation of Xanthomonas campestris (Fig. 2(a)). Its basic physicochemical properties are listed in Table 1. The SEM observations revealed that XG exhibited an irregular granular morphology under dry conditions, with uneven particle sizes and a rough surface texture (Fig. 2(b)).

The enzyme solution (ES) used in the EICP reaction was extracted from soybeans. The powdery soybean was dried at a low temperature, passed through a 10-mesh sieve, and then dissolved in distilled water to prepare a soybean solution with a concentration of 100 g/L. The solution was soaked at 4 °C for 24 h. Subsequently, it was centrifuged at 3000 r/min for 15 min to collect the supernatant, which served as the crude ES. The enzyme activity of ES under different environment was determined using the conductivity method [33]. As shown in Fig. 3, the enzyme activity increases with the pH increased within the pH range of 3 to 8.3, where the initial pH of the enzyme is 8.3. When the pH is below 4, enzyme activity remained below 5 mmol/(L·min) and increases only slightly. Particularly, when pH ⩽ 3.5, the activity drops below 2.5 mmol/(L·min), demonstrating the inactivation of enzyme. At the same time, temperature also has a significant effect on enzyme activity. At 0 °C,

(a) (b)

Fig. 2 Morphology of XG: (a) macroscopic morphology; (b) microscopic morphology.

Table 1 Basic physicochemical properties of XG

Chemical formula	Loss on drying (%)	Shearing ratio	1% XG in 1% KCl solution (cps)	Total plate count (cfu/g)
$C_8H_{14}Cl_2N_2O_2$	9.56	7.92	1425	800

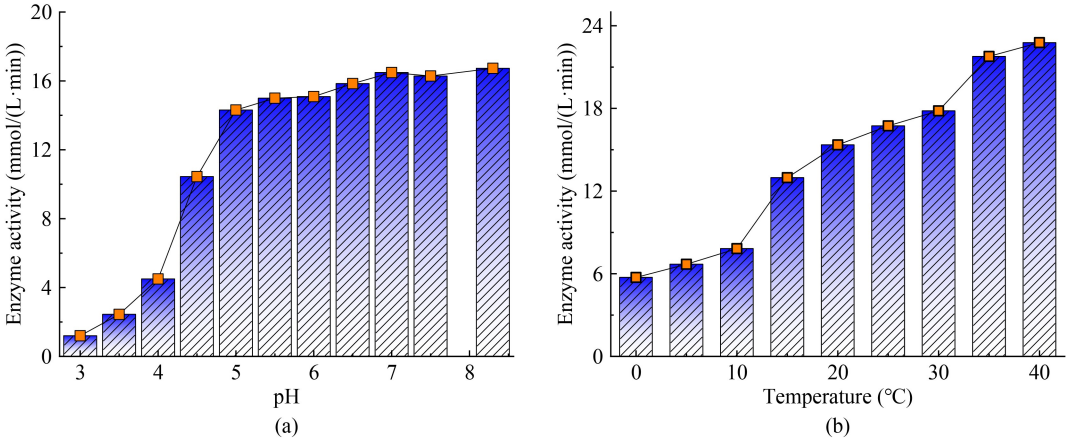

Fig. 3 Enzyme activity of the ES under different environment: (a) variation of enzyme activity with pH; (b) variation of enzyme activity with temperature.

the enzyme activity is approximately 6 mmol/(L·min), which is about one-third of that at room temperature (25 °C). With the increase of temperature, the enzyme activity increases and reaches 22.78 mmol/(L·min) at 40 °C. Although the enzyme activity at room temperature (16.73 mmol/(L·min)) is 6.05 mM/min lower than that at 40 °C, the operation under room temperature conditions eliminates the need for external heating, making the process simpler and more practical. Therefore, enzyme under room temperature conditions was used for grouting.

To investigate the influence of the biopolymer on the EICP, XG was added to the ES at the concentration of 0, 0.5, 1.0, 1.5, and 2.0 g/L. The mixtures were stirred thoroughly at 4 °C using a magnetic stirrer to ensure complete dissolution. After that, the ESs with XG were sealed and stored at 4 °C for subsequent use. The cementation solution (CS) used in the EICP consisted of urea and calcium acetate, both of which are white, powdery solids. Before the experiments, equimolar amounts of urea and calcium acetate were weighed, dissolved in distilled water, and stirred continuously for 30 min to form a CS with a molar concentration of 0.5 mol/L.

2.2 Specimen preparation

The specimen preparation process for biocemented sand is illustrated in Fig. 4. The mold consisted of an acrylic tube with an inner diameter of 5 cm, assembled with components including nuts, stainless steel gaskets, rubber stoppers, geotextiles, and exposure film. First, a perforated rubber stopper was used to seal the bottom of the tube, and a layer of geotextile was placed above it to prevent sand loss. Then, sand was placed into the mold in five layers using the layered compaction method. This process produced a cylindrical sand column with a dry density of 1.7 g/cm^3, a height of 10 cm, and a diameter of 5 cm. After that, the top of the specimen was covered with another piece of geotextile and sealed with a perforated rubber stopper. Finally, the upper and lower ends of the mold were secured using double-ended bolts.

The grouting system consisted of an air compressor, an air pressure control device, a reaction solution container, a support frame, and a beaker. A two-phase grouting method was employed as the following steps: First, an ES equivalent to 1.2 times the pore volume was grouted from the bottom of the mold under a grouting pressure of 20 kPa. The specimen was then left to stand for 2 h to allow sufficient adsorption of enzyme. As the two-phase grouting method replaces the ES with CS, the reaction efficiency is likely governed more by enzyme adsorption than by the ES-to-CS ratio. Hence, a CS of equal volume to the ES was subsequently injected under the same pressure, ensuring efficient enzyme replacement in soil pores while minimizing material consumption. Subsequently, a CS with the same volume of ES was grouted under the same pressure, and the leachate was collected by the beaker. The specimen was kept at room temperature (25 °C) for 24 h to allow the reaction. After 4 grouting cycles, distilled water equivalent to twice the pore volume was grouted to flush out residual ions and unreacted gel. The specimens were then demolded, and both ends were mechanically ground to obtain cylindrical specimens with regular dimensions and smooth, flat end surfaces. Meanwhile, all specimens were labeled according to the XG concentration. For instance, a specimen with an XG concentration of 2.0 g/L was designated as “XG20”.

2.3 Unconfined compressive strength tests

To evaluate the mechanical properties of the biocemented sand, UCS tests were conducted in accordance with ASTM D4219-11 [34]. The tests were performed using a

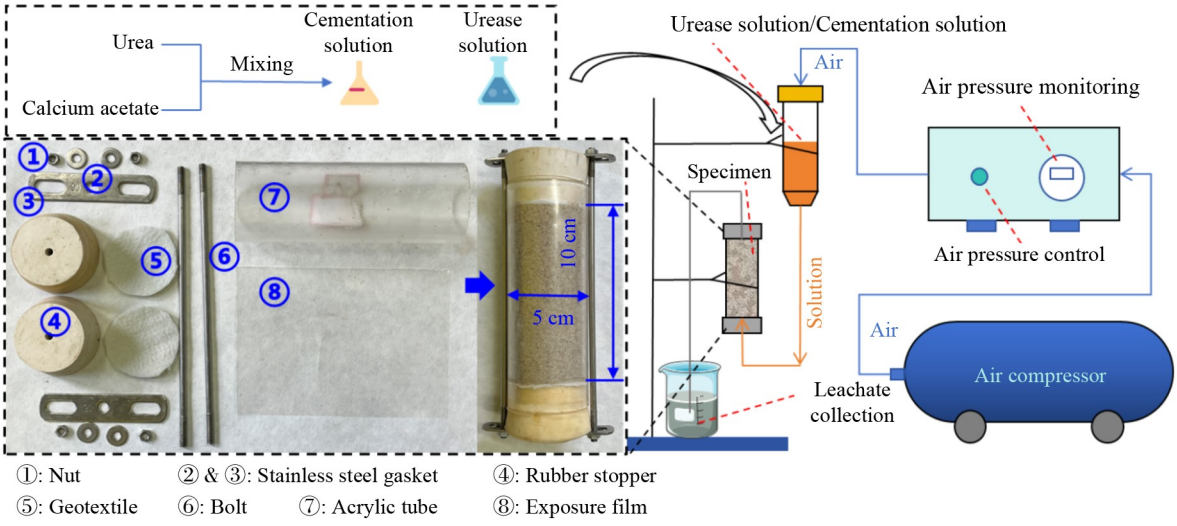

Fig. 4 Specimen preparation process for biocemented sand.

universal testing machine, applying axial load at a displacement rate of 1 mm/min until specimen failure occurred. During the tests, axial load and axial deformation were recorded to analyze the compressive strength and deformation characteristics of the specimens. After failure, each specimen was longitudinally divided into three equal sections from top to bottom and labeled as the upper section (U), middle section (M) and lower section (L), respectively. The samples were dried at 60 °C and were subsequently used for *CCC* measurement and microstructural analysis.

2.4 Measurements of calcium carbonate content

To evaluate the distribution characteristics of $CaCO_3$ during the variation of XG concentrations, the acid-washing method was employed to measure the *CCC* [7,35]. During the test, dried samples from the U, M, and L sections of each specimen were first finely ground, respectively. The powdered samples were then immersed in a HCl solution and allowed to react for 24 h until no bubbles were observed. After the reaction, the residual solids were filtered and thoroughly rinsed with deionized water to remove remaining acid and dissolved products. The samples were then dried in a constant-temperature oven at 60 °C for 24 h. The *CCC* was calculated as the percentage of $CaCO_3$ relative to the EICP-treated sand, as defined in Eq. (1):

$$CCC = \frac{m_1 - m_2}{m_1} \times 100\%, \tag{1}$$

where *CCC* denotes $CaCO_3$ content of biocemented sand (%), m_1 and m_2 denote the weight of samples before and after acid-washing (g), respectively.

2.5 Slaking resistance

In addition to evaluating the water stability of biocemented sand by measuring the UCS loss rate after immersion, UO tests have been used to evaluate the cementation of $CaCO_3$ under water-saturated conditions [8,36]. First, the dried biocemented samples were shaped into cubic blocks with an edge length of approximately 1.5 cm, then each cube was placed at the center of a black square tray to enhance contrast for image recognition. After that, the samples were immersed in an ultrasonic water bath and oscillations at a frequency of 40 kHz were applied for 10 min. During the test, a camera fixed in a top-down position captured images of the samples every minute to record their morphological changes. The captured images were processed using ImageJ software, as illustrated in Fig. 5. Initially, the images were converted to grayscale, followed by binarization, where the black area represented the sample, while the white area corresponded to the background. The number of black pixels was counted to determine the area of sample at each time point. Slaking resistance was characterized using the *SI* according to Xie et al. [37], as shown in Eq. (2):

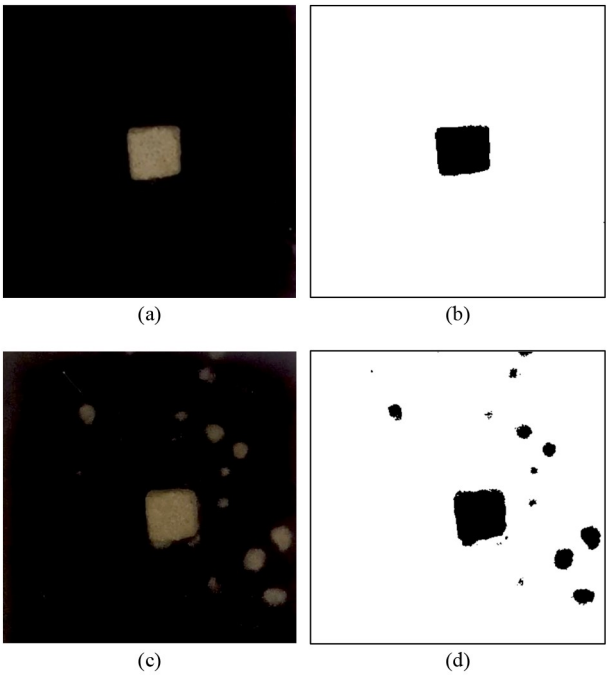

Fig. 5 Morphological changes of biocemented sand before and after UO tests: (a) sample before UO; (b) binarized image of sample before UO; (c) sample after 10 min of UO; (d) binarized image of sample after 10 min of UO.

$$SI = \frac{S_t}{S_0}, \tag{2}$$

where S_t denotes the area of sample at time t, S_0 denotes the area of sample before UO tests. A higher *SI* indicates a higher degree of slaking of biocemented sand.

2.6 Microscopic analysis

To further reveal the precipitation characteristics mineral composition of the $CaCO_3$ in biocemented sand, a series of microscopic analysis were carried out. Among them, some samples were shaped into cubic blocks with an edge length of approximately 1 cm, and their micromorphology was observed through using a FEI Quanta 250 scanning electron microscope. Simultaneously, the EDS was conducted to analyze the elemental composition and its spatial distribution. Furthermore, the formation patterns of $CaCO_3$ and its interfacial bonding with the soil skeleton particles were examined accordingly. Other samples were powdered and sieved for XRD analysis to identify the main mineral phases. The XRD tests were conducted using a D8-Discover X-ray diffractometer, and the diffraction patterns were analyzed using Jade software.

3 Results

3.1 Unconfined compressive strength tests analysis

Figure 6(a) illustrates the stress–strain curves of biocemented sand with different XG concentrations. It is seen that the specimens exhibit a typical stress–strain response characteristic of stabilized soils, consisting of the compaction stage, elastic deformation stage, plastic deformation stage, and failure stage [38,39]. Notably, specimens with higher XG concentrations display a sudden drop in stress after reaching the peak value, showing an obvious brittle failure behavior. Meanwhile, the UCS increases from 121.10 to 231.05 kPa as the XG concentration increases from 0 to 2 g/L, demonstrating the significant role of XG in enhancing the cementation efficiency of EICP. Furthermore, the failure strain exhibits a decreasing trend, further confirming the increased brittleness of biocemented sand [40–42]. Using only 0.5 mol/L CS for 4 rounds of grouting is sufficient to significantly enhance the soil strength, indicating good application potential in wind erosion control and soil-water conservation. For soil requiring higher strength, the number of grouting cycles and the $CaCl_2$ concentration can be further increased. In addition, compared with traditional chemical stabilizers, the EICP-based method provides better injectability, as both the ES and CS exhibit water-like fluidity, allowing them to penetrate soil pores more effectively than cement or lime slurry. Moreover, $CaCO_3$ is also the main constituent of natural limestone, thereby minimizing environmental disturbance [43–45].

The deformation modulus (E_{50}) is introduced as a representative parameter to evaluate the deformation behavior of different specimens, which corresponds to the secant slope of the stress–strain curve at 50% of the peak axial stress [46], as shown in Eq. (3):

$$E_{50} = \frac{\sigma_{1/2}}{\varepsilon_f/2}, \tag{3}$$

where $\sigma_{1/2}$ denotes the stress corresponding to 50% of the failure strain, ε_f denotes the failure strain.

The variation of UCS and E_{50} with XG concentration is illustrated in Fig. 6(b). It is seen that the UCS exhibits a two-stage growth trend with increasing XG concentration. When the XG concentration is below 1 g/L, the UCS increases from 121.10 to 152.82 kPa, exhibiting a 26.19% increase relative to the initial strength. In contrast, as XG

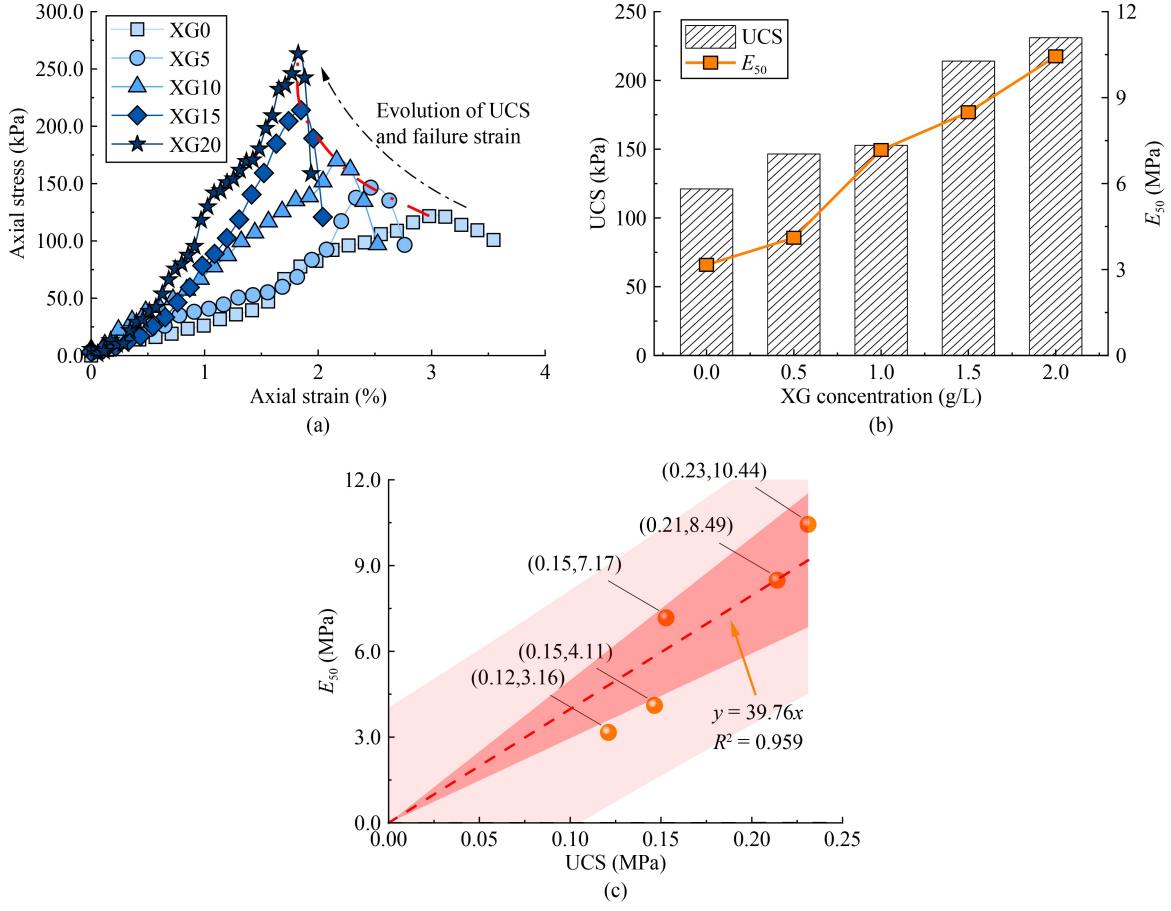

Fig. 6 Results of UCS tests: (a) stress–strain curve; (b) variation of UCS and E_{50} with XG concentration; (c) relationship between E_{50} and UCS.

concentration increases from 1 to 2 g/L, the UCS further rises to 231.05 kPa, exhibiting a 64.60% increase relative to the initial strength. The growth rate in the second stage is 2.47 times that of the first stage. This phenomenon may be attributed to the fact that at lower XG concentrations, the polymer plays an initial role in promoting nucleation. As the XG concentration further increases, the polymer chains begin to form a more complete network structure and more effectively adsorb Ca^{2+}, thereby facilitating the formation of additional $CaCO_3$. These $CaCO_3$ are then interconnected through the polymer network to form more stable bridging structures, resulting in a pronounced strength enhancement in the second growth stage [47,48].

On the other hand, E_{50} also increases with the increase of XG concentration, demonstrating that the addition of XG not only improves the UCS but also enhances the deformation resistance. As exhibited in Fig. 6(c), E_{50} increases with increasing UCS and a strong correlation is observed between the two parameters. The ratio of E_{50} to UCS is approximately 39.76, and the coefficient of determination (R^2) is 0.959.

3.2 Slaking resistance

As shown in Fig. 5, under the action of UO, the cementation between sand particles is disturbed, and the particles gradually detach from the matrix. Notably, the detached particles are mostly dispersed individually, indicating that the detachment process mainly occurs on the surface of the sample rather than complete structural failure. After 10 min of UO, the majority of the sample retained structural integrity. This phenomenon confirms the cementation formed by $CaCO_3$ provides a relatively high degree of stability and resistance to disturbance in water environment, further demonstrating the potential of microbially induced cementation in enhancing the slaking resistance of sand.

Figure 7 illustrates the time-dependent variation of *SI* at the U, M, and L sections of the specimens under different XG concentrations. The results indicate that the *SI* ranges between 1.0 and 3.0, showing an increasing trend with the increasing UO time. Notably, the most significant slaking occurs within the first 5 min, during which the *SI* increases by more than 70% of the total increment. After 5 min, the growth of *SI* slows down, and the disintegration process enters a relatively stable phase. This phenomenon is consistent with the Fig. 5 that the specimen largely retains its structural integrity after 10 min of UO, further confirming that the cementation formed by $CaCO_3$ exhibits excellent structural stability.

At the same XG concentration, the *SI* exhibits a gradually increasing trend from the bottom to the top of the specimen. This phenomenon can be attributed to the distribution of $CaCO_3$ under the two-phase grouting method: with the grouting of ES and CS from the bottom, $CaCO_3$ tends to precipitate in the lower part of the

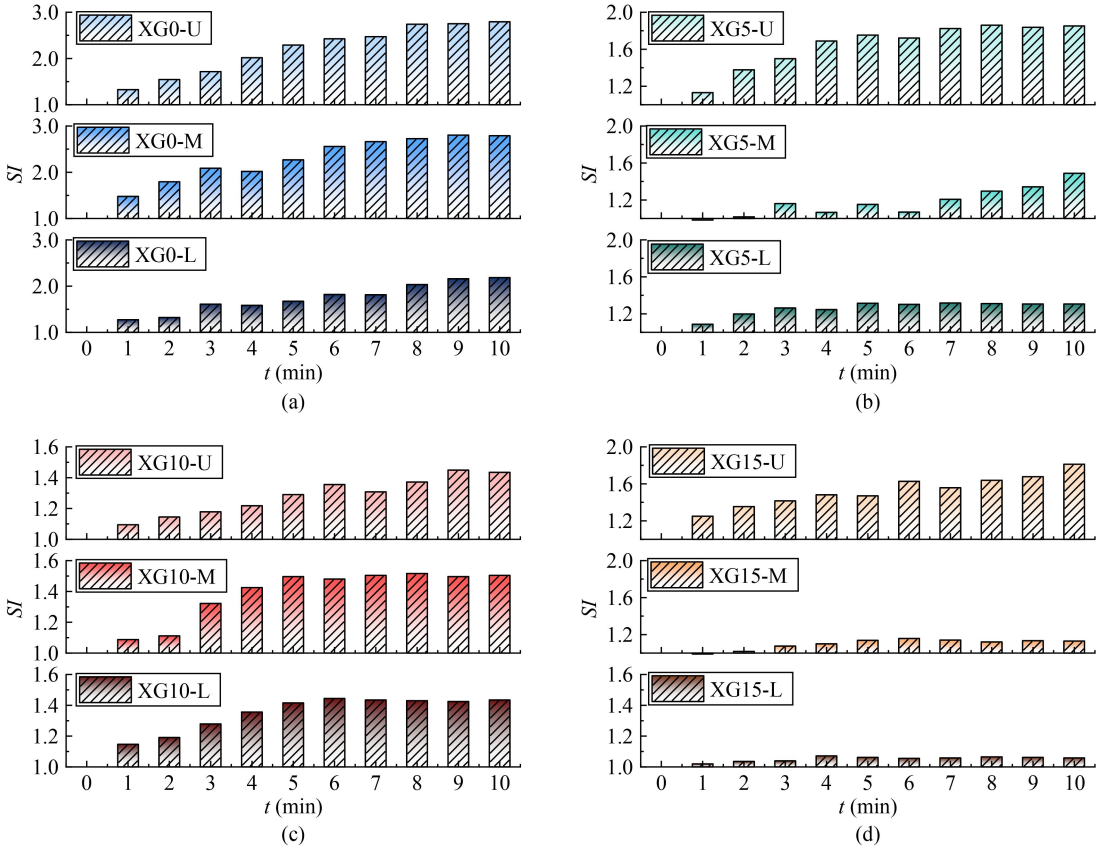

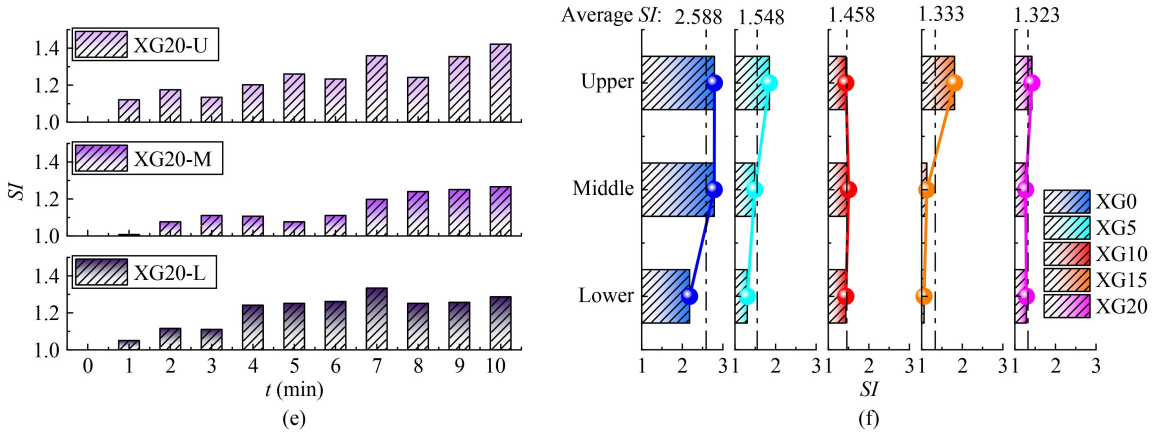

Fig. 7 Slaking behavior of biocemented sand under different conditions: (a) XG0; (b) XG5; (c) XG10; (d) XG15; (e) XG20; (f) variation of average *SI* with XG concentration.

specimen [49]. Consequently, the lower sections exhibit greater resistance to particle detachment under UO.

Figure 7 presents the variation of average *SI* with XG concentration after 10 min of UO. As the XG concentration increases from 0 to 2 g/L, the average *SI* decreases significantly from 2.588 to 1.323, demonstrating that the addition of XG improves the slaking resistance of biocemented sand in water environment. At the same time, this phenomenon indirectly reflects the strengthening effect of XG on inter-particle bonding, which is also one of the key factors contributing to the increase of UCS with increasing XG concentration. Furthermore, it is worth noting that XG can transforms into a colloidal gel that fills the pores between particles under saturated conditions [50], which will create a barrier effect to reduce the water intrusion and further improves the slaking resistance of the biocemented sand.

3.3 $CaCO_3$ content

The results of both the UCS tests and UO tests demonstrate that the addition of XG significantly enhances the mechanical properties and slaking resistance of the specimens. To further reveal the mechanism, quantitative analyses of *CCC* at different sections and under varying XG concentrations were conducted, the average *CCC* were also calculated, as shown in Fig. 8(a). It is seen that the *CCC* ranges from 1.36% to 2.32%, and increases from 1.477% to 2.179% as the XG concentration increases, demonstrating the nucleation-assist effect of XG on $CaCO_3$ precipitation. Under the same XG concentration, *CCC* exhibits a decreasing trend along the grouting direction (from bottom to top), which explains the previously observed increase in the *SI* with specimen height.

The homogeneity of the specimen can be evaluated using the statistical measures of standard deviation (S) and coefficient of variation (C_V), as defined in Eqs. (4) and (5) [51]:

$$S = \sqrt{\frac{1}{N}\sum_{1}^{N}(x_i - \bar{x})^2}, \tag{4}$$

$$C_V = \frac{S}{\bar{x}} \times 100\%, \tag{5}$$

where N denotes the number of samples, x_i denotes the *CCC* of the ith sample, and $\bar{x}$ denotes the average *CCC*. Higher values of S and C_V denote the lower homogeneity within the specimen.

The S and C_V of *CCC* under different XG concentrations is exhibited in Fig. 8(b). It is seen that when XG concentration is 0 g/L, the S and C_V are 0.111 and 7.540%, respectively. With the addition of XG, the S and C_V increase to ranges of 0.181–0.233 and 9.097%–12.103%, respectively, indicating a reduction of homogeneity of $CaCO_3$ distribution with the specimens under the action of XG. Furthermore, when the XG concentration exceeds 1 g/L, the *CCC* in the M and U sections of the specimens decreases more significantly. This distribution gradient can be attributed to the high viscosity of XG increases the flow resistance of the ES, resulting in a decrease in the retention of ES along the grouting direction [52], which accelerates the hydrolysis of urea at the bottom of the specimen during the grouting of the CS. As a result, the vertical gradient of *CCC* distribution becomes more obvious with increasing XG concentration.

Figures 8(c) and 8(d) further illustrate the correlations between *CCC* and both UCS and *SI*. The results indicate that UCS increases exponentially with increasing *CCC*, which is consistent with the findings reported by Sun et al. [53]. Conversely, *SI* exhibits an exponential decrease with increasing *CCC*, indicating that higher *CCC* significantly enhances the slaking resistance of the samples. The *CCC* plays a critical role in determining the mechanical and durability properties of biocemented sand, as well as XG contributes to a notable improvement in $CaCO_3$ precipitation. Hence, although the heterogeneous distribution of *CCC* induced by XG has begun to

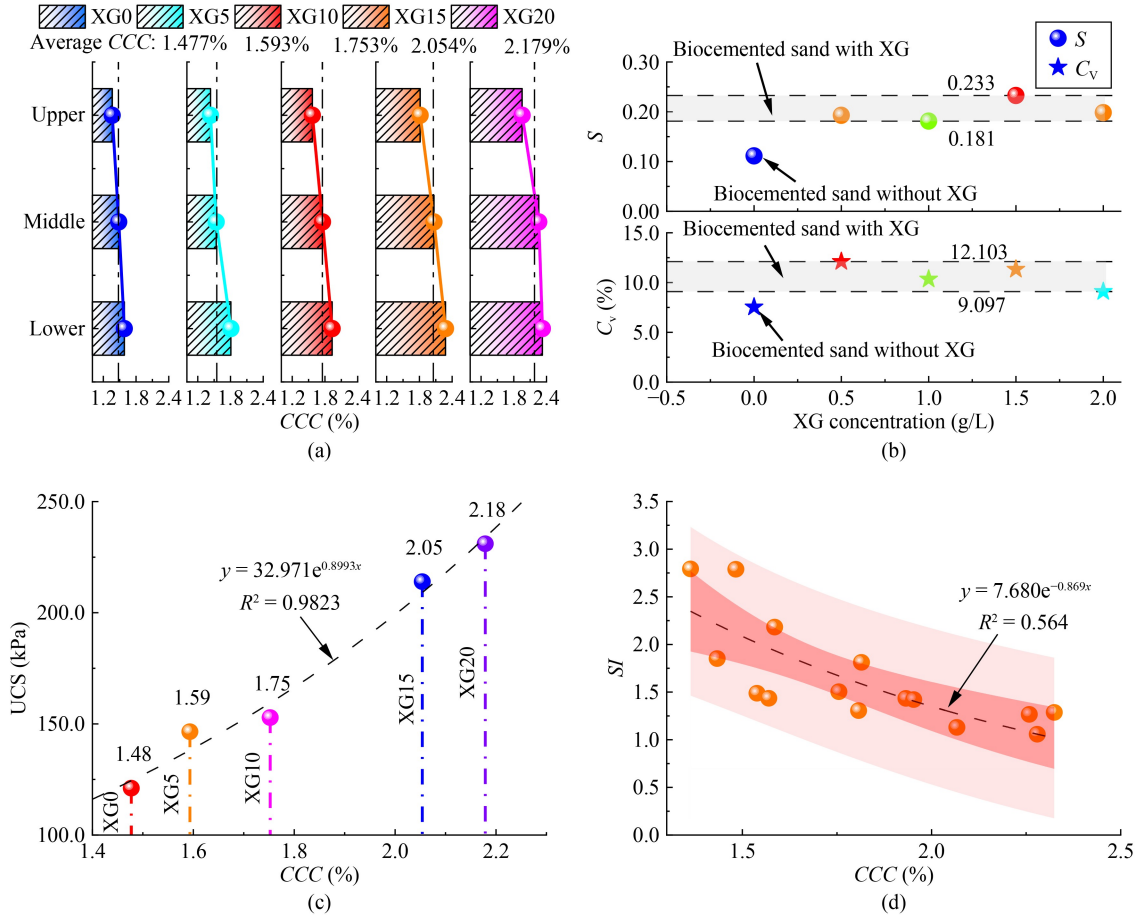

Fig. 8 Distribution characteristics of $CaCO_3$: (a) variation of *CCC*; (b) variation of *S* and C_V with XG concentration; (c) relationship between *CCC* and UCS; (d) relationship between *CCC* and *SI*.

emerge, its negative impact on the mechanical and slaking resistance remains insignificant within the scope of this study. Considering the heterogeneous distribution of *CCC* caused by XG carries a potential risk of evolving into structural defects. Therefore, future research should focus on optimizing the uniformity of $CaCO_3$ precipitation. Currently, various approaches have been proposed to improve the uniformity of EICP solidified soils during the grouting process, such as the low-pH method, low-temperature method, and the addition of inhibitors [8]. The combined effects of these techniques with XG on the distribution of $CaCO_3$ deserve further investigation.

3.4 Microscopic analysis

3.4.1 Scanning electron microscopy with energy-dispersive spectroscopy

Figure 9 presents the microstructure of biocemented sand with different XG concentrations at magnifications of 100 ×, 400 ×, and 1000 ×, where the morphology and distribution of $CaCO_3$ is observed. Due to the low low-energy at particle contact points and microscale surface indentations serve as preferential nucleation sites, $CaCO_3$ adheres to particle surfaces to form coatings or accumulates at contact points to create bridging structures, the cementation between particles is enhanced accordingly. For the samples without XG (Fig. 9(c)), the $CaCO_3$ precipitation is both insufficient in quantity and limited in crystal size. Consequently, few effective $CaCO_3$ crystals are formed at particle contacts, and uncemented gaps still remain between particles. On the contrary, with the increase of XG concentration, the amount of $CaCO_3$ crystals attached to particle surfaces increases accordingly, with larger crystal sizes observed (Figs. 9(f), 9(i), 9(l), and 9(o)). The precipitates gradually form larger aggregates at contact points, which almost fill the gap between particles.

This variation can be attributed to the physicochemical properties of XG itself. On the one hand, XG possesses high viscosity, enabling it to adsorb and accumulate in low-energy sites during the grouting, more ES is immobilized rather than be replaced by CS. On the other hand, XG adsorbs the Ca^{2+} in the CS due to its negative charge [54,55], promoting $CaCO_3$ precipitation at the attachment sites of ES. As a result, the precipitation of effective $CaCO_3$ is promoted in the biocemented sand.

Moreover, fibrous structures formed by XG under dry

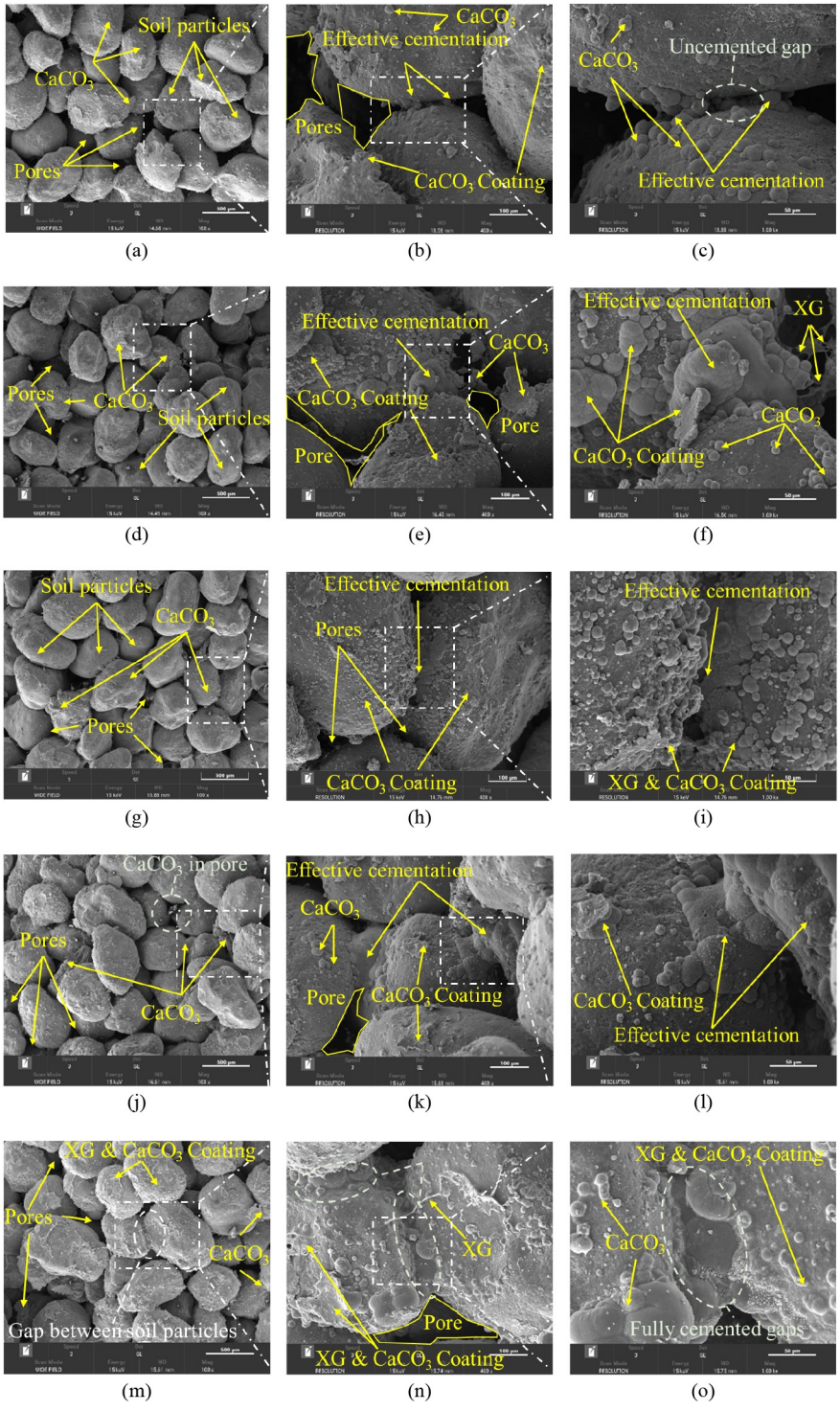

Fig. 9 Microstructure of biocemented sand with different XG concentrations: (a) XG0 100 ×; (b) XG0 400 ×; (c) XG0 1000 ×; (d) XG5 100 ×; (e) XG5 400 ×; (f) XG5 1000 ×; (g) XG10 100 ×; (h) XG10 400 ×; (i) XG10 1000 ×; (j) XG15 100 ×; (k) XG15 400 ×; (l) XG15 1000 ×; (m) XG20 100 ×; (n) XG20 400 ×; (o) XG20 1000 ×.

conditions can be observed on particle surfaces and pores, as shown in Figs. 9(f) and 9(n). Under such condition, XG may enhance soil strength by establishing fibrous connections between particles. Whereas in saturated conditions, it swells into a hydrogel that fills the pores and prevent the water erosion. Considering the strong cementation effect of $CaCO_3$ and the low concentration of XG, the strength enhancement due to fiber formation can be ignored. Therefore, the primary functions of XG are promoting the precipitation of $CaCO_3$ through enzyme immobilization and filling pores under saturated conditions.

The elemental distribution at the particle interfaces of XG0, XG10, and XG20 is analyzed using EDS, the results are shown in Fig. 10. Based on the chemical compositions of sand and reactants, Ca is identified as a key indicator of $CaCO_3$. Ca is distributed on the surfaces of sand particles and at particle contact points. In the sample without XG, the Ca content is measured at only 6.51% by EDS, and the spatial distribution of Ca

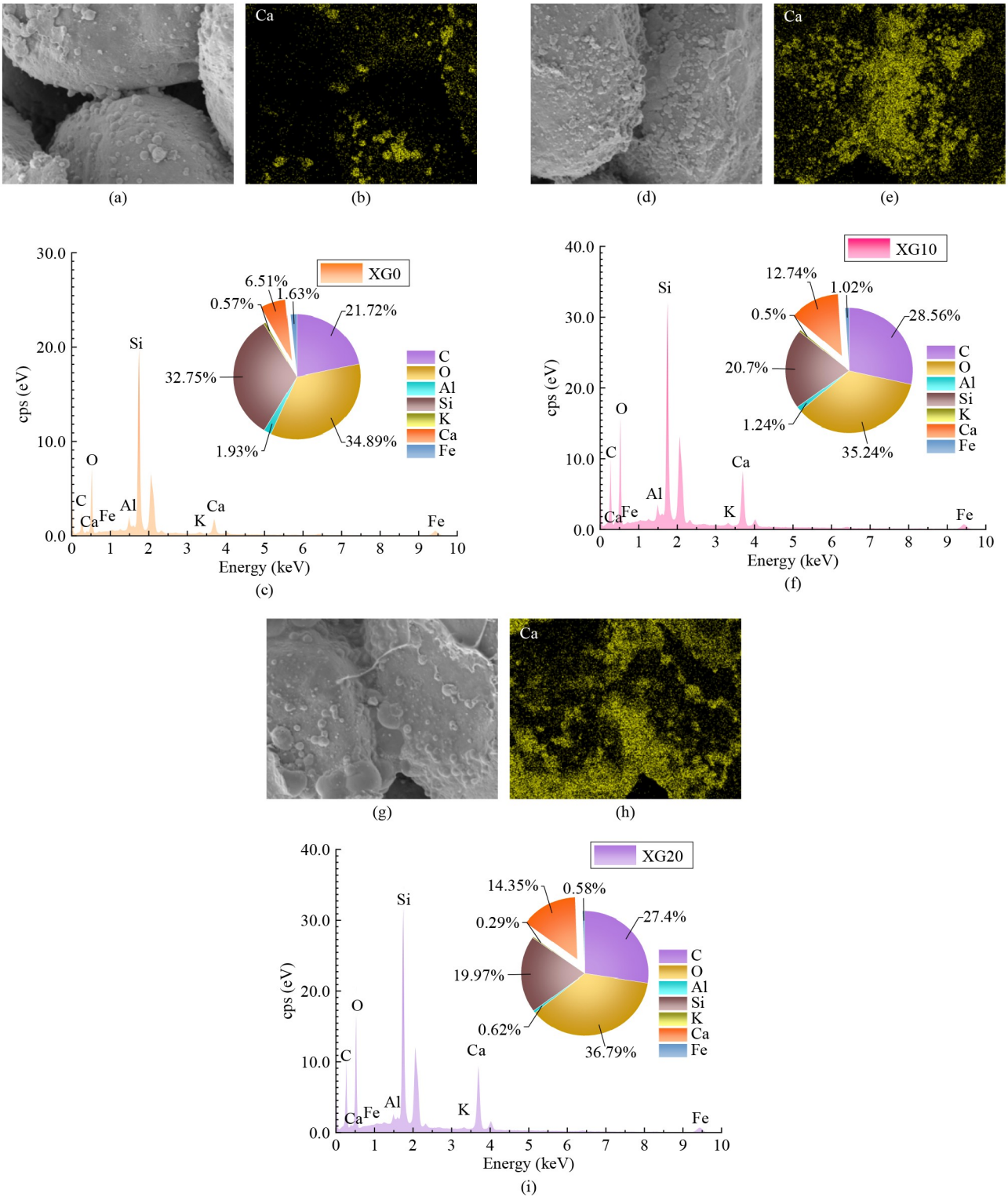

Fig. 10 Elemental distribution at the particle interfaces of biocemented sand: (a) microstructure of XG0; (b) Ca distribution of XG0; (c) EDS spectrum of XG0; (d) microstructure of XG10; (e) Ca distribution of XG10; (f) EDS spectrum of XG10; (g) microstructure of XG20; (h) Ca distribution of XG20; (i) EDS spectrum of XG20.

appeared sparse due to the relatively low efficiency of $CaCO_3$ precipitation. With the increase of XG concentration, EDS images show notably Ca accumulation on particle surfaces, especially at contact points between particles. Consequently, when the XG concentration rises to 2 g/L, the Ca content increases to 14.35% accordingly.

The EDS results indicate that with the assistance of XG, larger $CaCO_3$ agglomerates and thicker $CaCO_3$ coatings were formed, improving the bonding between particles significantly. The findings further explain the reason that the addition of XG enhances the mechanical strength and slaking resistance of the biocemented sand.

3.4.2 X-ray diffraction

Figure 11 presents the XRD patterns of biocemented sand with different XG concentrations. Due to the high sand content (exceeding 95%), obvious diffraction peaks of SiO_2 are observed in the pattern. In addition, the main crystalline forms of $CaCO_3$ generated by EICP are recognized as calcite and vaterite, with calcite showing stronger peak intensities than vaterite. Calcite is known for its more compact crystal structure, higher crystallinity, and superior bonding ability, thus contributing more effectively to cementation between particles [36,56].

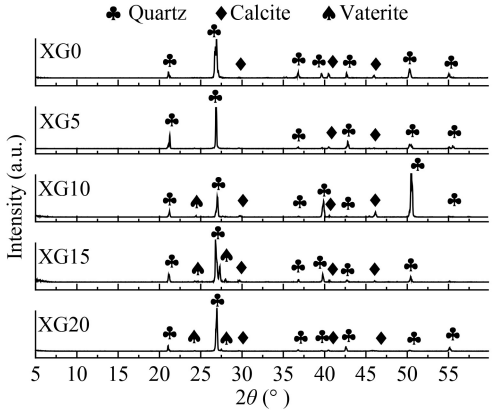

Fig. 11 XRD patterns of biocemented sand.

With increasing of XG concentration, a noticeable enhancement in the vaterite peak intensity is observed. This phenomenon may be attributed to the influence of XG that inhibits the transformation of vaterite into calcite [57,58]. Despite minor variations in the crystalline composition, the $CaCO_3$ content increases obviously with higher XG concentrations, and the influence of crystal phase on biocemented sand still limited. Aas a result, the UCS and *SI* still increase with XG concentration increased.

4 Discussion

4.1 Mechanism of xanthan gum-assisted $CaCO_3$ nucleation

XG is a kind of extracellular polymeric substance produced from Xanthomonas campestris, its primary molecular structure is illustrated in Fig. 12 [59]. It is seen that the is primarily composed of D-glucose, D-mannose, and D-glucuronic acid in an approximate molar ratio of 2:2:1. Its main chain is composed of β-D-glucose, while the side chains are composed of D-mannose and glucuronic acid. The molecule is a characteristic right-handed 5-fold helical secondary configuration. Owing to its unique molecular configuration, XG exhibits a range of exceptional properties, including high viscosity, excellent rheological behavior, superior freeze–thaw stability, and extremely low toxicity [27].

The cementation mechanisms of sand under different reinforcement methods are illustrated in Fig. 13. SEM

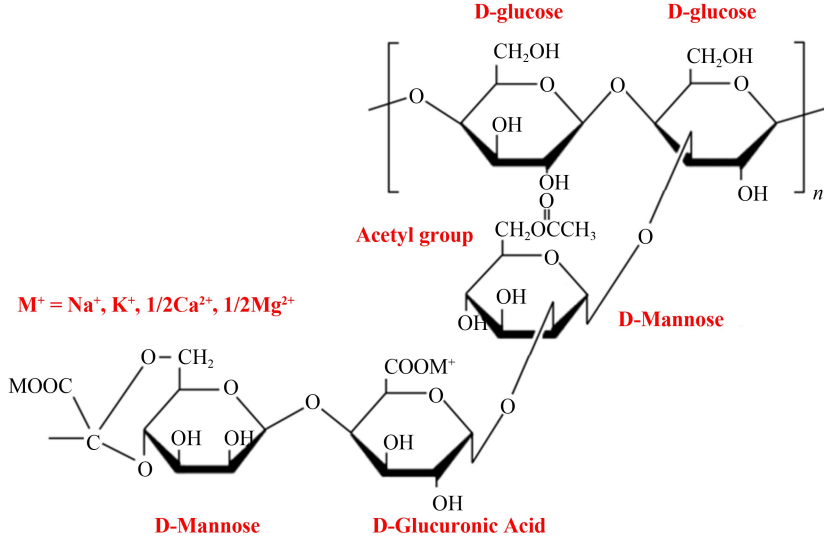

Fig. 12 Primary molecular structure of XG.

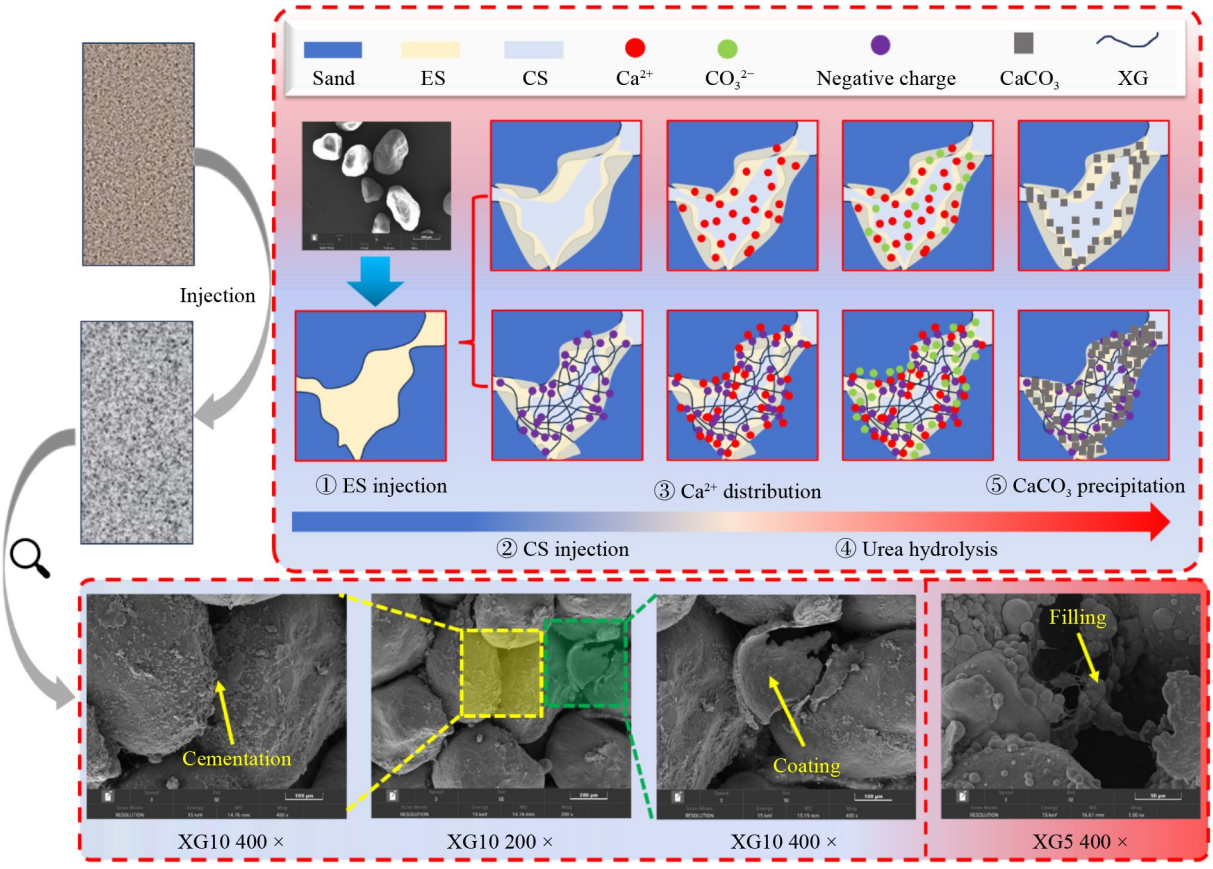

Fig. 13 Cementation mechanisms of sand under different reinforcement methods.

images confirm that in EICP-treated sand, $CaCO_3$ exists with three morphological forms: interparticle bonding at contact points, surface coating on sand surfaces, and filling pores between particles. During the grouting of ES, the pores are first saturated by it. Due to the surface depressions, the low-energy sites are mainly at particle depressions and contact areas. Hence, although the ES within the pores is gradually displaced during the grouting of CS, several ES is still retained at the low-energy sites, and $CaCO_3$ prefers to precipitate at these specific sites first. In terms of biocemented sand without XG, the ES exhibits low viscosity and weak adsorption, the reaction system lacks nucleation sites. Consequently, the efficiency of $CaCO_3$ precipitation is reduced, the dispersed and ineffective free $CaCO_3$ is more likely to form. This phenomenon corresponds with the sparse distribution of Ca observed in Fig. 10(b).

With the addition of XG, the viscosity of the ES increases significantly. Under the influence of matrix suction, more ES is retained at low-energy sites during grouting [60], reducing the probability of being displaced by CS. Moreover, XG molecules contain terminal glucuronic acid and carboxylate groups, which guarantee a high degree of negative charge (Fig. 12), thereby enhancing their ability to adsorb Ca^{2+} ions [61]. Due to the additional nucleation sites provided by XG, more $CaCO_3$ prefers to precipitate and accumulate on particle surfaces and at contact points, improving effective cementation between particles. Hence, it can be considered that the addition of XG enhances the workability of biocemented sand by optimizing the distribution and deposition efficiency of $CaCO_3$.

4.2 Slaking behavior of biocemented sand under ultrasonic oscillation

Figure 14 illustrates the schematic of the slaking process of the biocemented sand under UO. The relative stability between sand particles is primarily provided by the presence of effective $CaCO_3$. Under the disturbance of ultrasonic, the cementation between particles is destroyed. Since the surface sand particles are less constrained by $CaCO_3$ compared to those inner the samples, the surface particles and the bonded $CaCO_3$ detach first. Subsequently, as the outer layer detaches, the internal particles experience a reduced constraint, and the sample experiences a progressive slaking from the exterior to the interior. According to the relationship between *CCC* and the *SI* established in Fig. 8(d), specimens with higher *CCC* exhibit stronger cementation than those with lower *CCC*. Due to the generation of effective $CaCO_3$ increases with higher XG concentrations, the samples with higher XG obtain lower *SI* under UO accordingly.

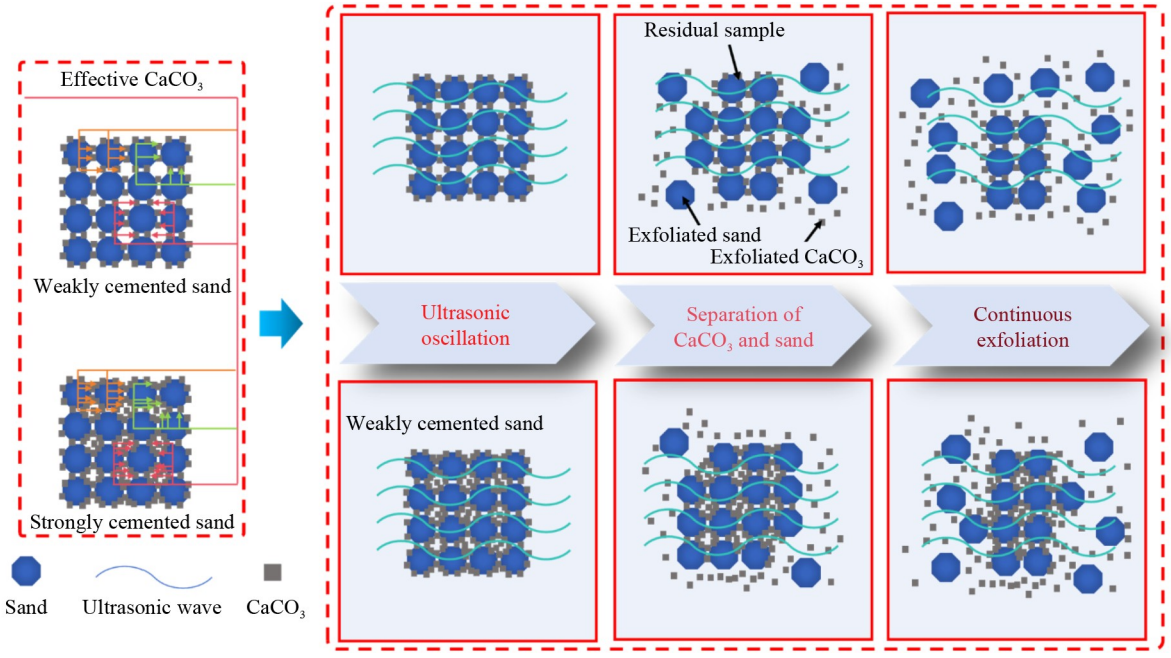

Fig. 14 Slaking process of biocemented sand under UO.

5 Conclusions

In this study, the sand was cemented using XG-immobilized enzyme to assist $CaCO_3$ nucleation. The mechanical properties and slaking resistance of biocemented sand were evaluated, and microscopic analysis were further conducted to reveal the XG-assisted nucleation mechanism. This provides a foundation for improving the $CaCO_3$ nucleation efficiency of biocementation technology in erosion control and hydrological engineering. The main conclusions are as follows.

1) XG exhibits a significant assisting effect on $CaCO_3$ nucleation. As the XG concentration increased from 0 to 2 g/L, the UCS of the biocemented sand increased from 121.10 to 231.05 kPa after 4 cycles of grouting, exhibiting a strength increase of 90.8%. The E_{50} also increased correspondingly with XG content and showed a strong linear correlation with UCS

2) The *SI* of biocemented sand ranges from 1.0 to 3.0 and showed an increase along the grouting direction, which is attributed to the inhomogeneous distribution of $CaCO_3$. As the XG concentration increased from 0 to 2 g/L, the average *SI* decreased from 2.588 to 1.323, showing an increasing slaking resistance with the addition of XG.

3) The UCS exhibits an exponential increase with the increase of *CCC*, whereas the *SI* decreases exponentially, confirming that *CCC* is the main parameter that controls the performance of biocemented sand. XG enhances the mechanical and slaking resistance properties of the biocemented sand by promoting the formation of effective $CaCO_3$. However, the high viscosity of XG increases the inhomogeneous distribution of $CaCO_3$, further optimization is needed to balance the cementation and homogeneity.

4) EDS results indicate that the Ca content rises from 6.51% to 14.35% as the XG concentration increases from 0 to 2 g/L. $CaCO_3$ accumulated at particle contacts and surfaces, forming larger $CaCO_3$ clusters between particle contact points, which are the microstructural basis for the improvement in strength and slaking resistance of biocemented sand caused by the addition of XG.

5) The mechanism of XG-assisted $CaCO_3$ nucleation lies in two synergistic effects: first, the viscosity of ES increases with XG addition, enabling greater ES retention at low-energy sites during grouting; second, the negatively charged functional groups on XG significantly enhance Ca^{2+} adsorption, providing nucleation sites for the precipitation of $CaCO_3$ at particle contact points, thereby improving the cementation efficiency of EICP.

Acknowledgements This study was partially supported by the National Natural Science Foundation of China (Grant No. 52378330) and SEU Innovation Capability Enhancement Plan for Doctoral Students (No. CXJH_SEU 24202)), which are essential to the successful completion of this manuscript.

Competing interests The authors declare that they have no competing interests.

References

1. Li S Q, Yang Z P, Gao Y H, Liu X R, Jin X G. The effect of clay swelling on crack generation in red stratum soft rock during water-

induced disintegration: A matrix-based discrete element simulation study. Bulletin of Engineering Geology and the Environment, 2024, 83: 489
2. Zhang S, Jiao N, Ding J W, Guo C, Gao P J, Wei X. Utilization of waste marine dredged clay in preparing controlled low strength materials with polycarboxylate superplasticizer and ground granulated blast furnace slag. Journal of Building Engineering, 2023, 76: 107351
3. Cheng Y J, Tang C S, Pan X H, Liu B, Xie Y H, Cheng Q, Shi B. Application of microbial induced carbonate precipitation for loess surface erosion control. Engineering Geology, 2021, 294: 106387
4. Sartori M, Ferrari E, M'Barek R, Philippidis G, Boysen-Urban K, Borrelli P, Montanarella L, Panagos P. Remaining loyal to our soil: A prospective integrated assessment of soil erosion on global food security. Ecological Economics, 2024, 219: 108103
5. Tang C S, Pan X H, Cheng Y J, Ji X L. Improving hydro-mechanical behavior of loess by a bio-strategy. Biogeotechnics, 2023, 1(2): 100024
6. Yu X N, Pan X H. One-phase stabilization of sandy soil using seawater-based soybean induced carbonate precipitation. Journal of Sustainable Cement-Based Materials, 2023, 12(8): 962–971
7. Cheng L, Shahin M A, Chu J. Soil bio-cementation using a new one-phase low-pH injection method. Acta Geotechnica, 2019, 14(3): 615–626
8. Zhang S, Ding J W, Wang S J, Li C H. Evaluation of calcium carbonate production and cementitious characteristics of enzymatically induced carbonate precipitation during environmental adjustment. Construction & Building Materials, 2024, 449: 138415
9. Xu J, Wang X Z, Yao W, Kulminskaya A A, Shah S P. Microbial-inspired self-healing of concrete cracks by sodium silicate-coated recycled concrete aggregates served as bacterial carrier. Frontiers of Structural and Civil Engineering, 2024, 18(1): 14–29
10. Liu H L, Zhao C, Xiao Y. Reaction principle, deposition and failure mechanisms and theory of biomineralization: Progress and challenges. Chinese Journal of Geotechnical Engineering, 2024, 46(7): 1347–1358 (in Chinese)
11. Whiffin V S, van Paassen L A, Harkes M P. Microbial carbonate precipitation as a soil improvement technique. Geomicrobiology Journal, 2007, 24(5): 417–423
12. Hou J, Zhang M Z, Wang P F, Wang C, Miao L Z, Xu Y, You G X, Lv B W, Yang Y Y, Liu Z L. Transport and long-term release behavior of polymer-coated silver nanoparticles in saturated quartz sand: The impacts of input concentration, grain size and flow rate. Water Research, 2017, 127(15): 86–95
13. Nawarathna T H K, Nakashima K, Kawasaki S. Chitosan enhances calcium carbonate precipitation and solidification mediated by bacteria. International Journal of Biological Macromolecules, 2019, 133: 867–874
14. Ma G L, He X, Jiang X, Liu H L, Chu J, Xiao Y. Strength and permeability of bentonite-assisted biocemented coarse sand. Canadian Geotechnical Journal, 2021, 58: 969–981
15. Refaei M, Arab M G, Omar M. Sandy soil improvement through biopolymer assisted EICP. American Society of Civil Engineers, 2020, 612–619
16. Tasuji M R A, Ghadir P, Hosseini A, Javadi A A, Korayem A H, Ranjbar N. Experimental investigation of sandy soil stabilization using chitosan biopolymer. Transportation Geotechnics, 2024, 46: 101266
17. Cui M, Xiong H H, Zheng J J, Cui M J, Lv S Y, Han S Y. Strength investigation of sand treated by enzyme-induced carbonate precipitation combined with chitosan. International Journal of Geomechanics, 2024, 24(6): 04024098
18. Wei S P, Xiao F R, Dong H Z, Chen H J. Carbonate polymorph formation in microbially induced calcium carbonate precipitation (MICP): Influencing factors, mechanisms, and knowledge gaps. Earth-Science Reviews, 2025, 265: 105129
19. Lai H J, Wu S F, Cui M J, Chu J. Recent development in biogeotechnology and its engineering applications. Frontiers of Structural and Civil Engineering, 2021, 15(5): 1073–1096
20. DeJong J T, Fritzges M B, Nüsslein K. Microbially induced cementation to control sand response to undrained shear. Journal of Geotechnical and Geoenvironmental Engineering, 2006, 132(11): 1381–1392
21. Wei Y, Xu H, Xu S, Su H, Sun R, Huang D, Zhao L Q, Hu Y C, Wang K Q, Liao X J. Synthesis and characterization of calcium carbonate on three kinds of microbial cells templates. Journal of Crystal Growth, 2020, 547: 1–7
22. Woolley M A, van Paassen L A, Kavazanjian E J. Impact on surface hydraulic conductivity of eicp treatment for fugitive dust mitigation. In: Geo-Congress 2020: Biogeotechnics. Reston, VA: American Society of Civil Engineers, 2020, 132–140
23. Bian X, Zhao F Y, Zeng L L, Ren Z L, Li X Z. Role of superabsorbent polymer in compression behavior of high-water-content slurries. Acta Geotechnica, 2024, 19: 6163–6178
24. Cui M, Xiong H H, Zheng J J, Cui M J, Lv S Y, Lai H J. Experimental study on multiscale engineering properties of EICP combined with xanthan gum solidified sand. Journal of Materials in Civil Engineering, 2024, 36(6): 04024108
25. Moghal A A B, Vydehi K V. State-of-the-art review on efficacy of xanthan gum and guar gum inclusion on the engineering behavior of soils. Innovative Infrastructure Solutions, 2021, 6: 108
26. Xiao Y, Fang Q, He X, Cui H, Ge J, Liu H. Strength of biocemented sand-EPS mixtures. Journal of Rock Mechanics and Geotechnical, 2026 (in press)
27. Kang J, Yue H X, Li X X, He C, Li Q, Cheng L T, Zhang J X, Liu Y, Wang S J, Guo Q B. Structural, rheological and functional properties of ultrasonic treated xanthan gums. International Journal of Biological Macromolecules, 2023, 246: 125650
28. Ouyang M, Zhang H, Deng R R, Wang G Y, Xiao J, Zhao Y. Development of cracks in expansive soil improved by xanthan gum biopolymer. Chinese Journal of Geotechnical Engineering, 2025, 47(1): 106–114 (in Chinese)
29. Xiao Y, Fu G Y, Shi J Q, Huang X L, Cui H, Liu H L. Bio-hydrogel and biomineralization in improving water retention ability of sandy soils. Acta Geotechnica, 2025, 20: 4589–4597
30. Hang L, Van Paassen L A, Ehsasi F, Chen Y B, Li R R, He J. An experimental investigation on use of xanthan gum biopolymer as additive for improving the reinforcement effect of biocementation on sandy soils. Geomicrobiology Journal, 2024, 41(6): 627–635
31. Kumar M A, Moghal A A B, Rasheed R M, Rehman, A U. Enhancing durability and erosion resistance of soils with varying plasticity using crosslinked biopolymers. Scientific Reports, 2025,

15: 12572
32. ASTM. Standard Test Method for Particle-size Analysis of Soils, ASTM D422-63. West Conshohocken, PA: ASTM, 2007
33. Whiffin V S. Microbial $CaCO_3$ precipitation for the production of biocement. Dissertation for the Doctoral Degree. Perth West Australia: Murdoch University, 2004
34. ASTM. Standard Test Method for Unconfined Compressive Strength Index of Chemical-Grouted Soils, ASTM D4219-11. West Conshohocken, PA: ASTM, 2011
35. Gao Y F, Hang L, He J, Chu J. Mechanical behaviour of biocemented sands at various treatment levels and relative densities. Acta Geotechnica, 2019, 14: 697–707
36. Lv C, Tang C S, Zhang J Z, Zhu C, Pan X H, Liu H. Environmental dependence of microbially induced calcium carbonate crystal precipitations: Experimental evidence and insights. Journal of Geotechnical and Geoenvironmental Engineering, 2022, 148(7): 04022050
37. Xie Y H, Tang C S, Liu B, Cheng Q, Yin L Y, Jiang N J, Shi B. Water stability improvement of clayey soil based on microbial induced calcite precipitation. Journal of Zhejiang University (Engineering Science), 2019, 53(8): 1438–1447
38. Liu L, Liu H L, Stuedlein A W, Evans T M, Xiao Y. Strength, stiffness, and microstructure characteristics of biocemented calcareous sand. Canadian Geotechnical Journal, 2019, 56(10): 1502–1513
39. Li C, Bai S R G L, Zhou T J, Liu H L, Qin X, Liu S H, Liu X Y, Xiao Y. Strength-increase mechanism and microstructural characteristics of a biotreated geomaterial. Frontiers of Structural and Civil Engineering, 2020, 14(3): 599–608
40. Xiao Y, He X, Ma G L, Zhao C, Chu J, Liu H L. Biomineralization and mineralization using microfluidics: A comparison study. Journal of Rock Mechanics and Geotechnical Engineering, 2024, 16(2): 661–669
41. Jiang X L, Wang H D, Yang H, Du T, Liu P, Duan J X. Triaxial compression characteristics and brittleness evaluation of calcareous sand cemented with EICP and coir fiber. Results in Engineering, 2025, 25: 104090
42. Xiao Y, He X, Evans T M, Stuedlein A W, Liu H L. Unconfined compressive and splitting tensile strength of basalt fiber-reinforced biocemented sand. Journal of Geotechnical and Geoenvironmental Engineering, 2019, 145(9): 04019048
43. Bian X, Xiao J Y, Zhang T, Zeng L L. Mitigating acid rain effects on stabilized soils: The role of phosphogypsum in leaching resistance. Journal of Rock Mechanics and Geotechnical Engineering, 2025 (in press)
44. He B, Yue P, Zhu Y Q, Liu H Y, Guo Z, Li Y J. Experimental study on hole erosion behaviors of marine soil solidified by an innovative organic composite material. Applied Ocean Research, 2025, 163: 104755
45. Xiao Y, He X, Wu W, Stuedlein A W, Evans T M, Chu J, Liu H L, van Paassen L A, Wu H R. Kinetic biomineralization through microfluidic chip tests. Acta Geotechnica, 2021, 16(10): 3229–3237
46. Zhang S, Ding J W, Liu J Y, Gao M Y, Xue C R. Al_2O_3/SO_3 molar ratio of PG-CAC-based binders on the macro-micro properties of cement-treated waste dredged clay. Construction & Building Materials, 2024, 424: 135950
47. Vydehi K V, Moghal A A B. Effect of biopolymeric stabilization on the strength and compressibility characteristics of cohesive soil. Journal of Materials in Civil Engineering, 2022, 34(2): 04021450
48. Li Y J, Guo Z, Wang L Z, Zhu Y Q, Rui S J. Field implementation to resist coastal erosion of sandy slope by eco-friendly methods. Coastal Engineering, 2024, 189: 104489
49. Lai H J, Cui M J, Chu J. Effect of pH on soil improvement using one-phase-low-pH MICP or EICP biocementation method. Acta Geotechnica, 2023, 18: 3259–3272
50. Thombare N, Mishra S, Siddiqui M Z, Jha U, Singh D, Mahajan G R. Design and development of guar gum based novel, superabsorbent and moisture retaining hydrogels for agricultural applications. Carbohydrate Polymers, 2018, 185: 169–178
51. Jia J, Wan Y, Liu H, Qi K, Zhang J. Evaluation of compaction uniformity of the paving layer based on transverse and longitudinal measurements. International Journal of Pavement Engineering, 2019, 22(187): 1–13
52. Cui M J, Lai H J, Hoang T, Chu J. One-phase-low-pH enzyme induced carbonate precipitation (EICP) method for soil improvement. Acta Geotechnica, 2021, 16: 481–489
53. Sun X H, Miao L C, Wang H X, Guo X, Wu L Y. Control of urease activity in enzyme-induced carbonate precipitation method for soil improvement at high temperatures. Acta Geotechnica, 2024, 19: 7495–7515
54. Zhang K, Tang C S, Jiang N J, Pan X H, Liu B, Wang Y J, Shi B. Microbial-induced carbonate precipitation (MICP) technology: A review on the fundamentals and engineering applications. Environmental Earth Sciences, 2023, 82(9): 229
55. Liu Y, Ali A, Su J F, Li K, Hu R Z, Wang Z. Microbial-induced calcium carbonate precipitation: Influencing factors, nucleation pathways, and application in wastewater remediation. Science of the Total Environment, 2023, 860: 160439
56. Xu K, Huang M, Cui M J, Li S. Retarding effect of cementation solution concentration on cementation ability of calcium carbonate crystal induced using crude soybean enzyme. Acta Geotechnica, 2023, 18: 6235–6251
57. Kosanović C, Fermani S, Falini G, Kralj D. Crystallization of calcium carbonate in alginate and xanthan hydrogels. Crystals, 2017, 7(12): 355
58. Xu W, Liu H, Lou Y C, Jin W P, Xue X N, Liu X F, Yang N N. Biomimetic mineralization of calcium carbonate using xanthan gum as morphology control agent. Micro & Nano Letters, 2019, 14(6): 642–644
59. Xu L, Xu G Y, Liu T, Chen Y J, Gong H J. The comparison of rheological properties of aqueous welan gum and xanthan gum solutions. Carbohydrate Polymers, 2013, 92(1): 516–522
60. DeJong J T, Mortensen B M, Martinez B C, Nelson D C. Bio-mediated soil improvement. Ecological Engineering, 2010, 36: 197–210
61. Mohamed A M O, O'Kelly B C, Soltani A. Sustainability in ground improvement: The case of xanthan gum biopolymer. Cham: Springer, 2024